A diselenide MOF-based nanomotor dual-driven by carbon monoxide and near-infrared-II light for multimodal tumor-targeted therapy

Ruizhen Tian, Zherui Zhang, Liping Song, Yijia Li, Zhengwei Xu, Wang Liu, Tianlong Zhang, Jiayun Xu, Youju, Huang, Tingting Wang, Xiaotong Fan* and Junqiu Liu**

R. Z. Tian, Z. R. Zhang, L. P. Song, Y. J. Li, Z. W. Xu, W. Liu, T. L. Zhang, J. Y. Xu, T. T. Wang, S. J. Yu, Y. J. Huang, J. Q. Liu
College of Material, Chemistry and Chemical Engineering, Key Laboratory of Organosilicon Chemistry and Material Technology, Ministry of Education, Hangzhou Normal University, Hangzhou 311121, China;
E-mail: junqiuliu@jlu.edu.cn, wangtt@hznu.edu.cn

X. T. Fan
Institute of Sustainability for Chemicals, Energy and Environment (ISCE2), Agency for Science, Technology and Research (A*STAR), 1 Pesek Road, Jurong Island,
Singapore 627833, Republic of Singapore.
Email: xiaotong_fan@isce2.a-star.edu.sg

Keywords: dual-driven nanomotors, diselenide metal-organic frameworks, CO release, NIR-II light-responsive mild photothermal therapy, chemodynamic therapy, starvation therapy,

The dense extracellular matrix and high interstitial pressure within tumors hinder nanoparticle penetration, reducing therapeutic efficacy. To address this, we engineered a dual-driven nanomotor based on a diselenide metal-organic framework (MOF) using a layer-by-layer assembly process for multimodal synergistic tumor therapy. Diselenide-containing imidazole derivatives coordinated with Zn^{2+} form the MOF, sequentially encapsulating NIR-II photothermal-responsive gold nanorods (AuRods), Mn_2CO_{10} (MnCO), and glucose oxidase (GOD). The nanoparticle surface was functionalized with 4T1 cancer cell membranes (DSACGM NPs), providing direction for the nanomotors to drive toward the tumor site. The photothermal effect of AuRods and CO release drives nanomotor propulsion, enhancing tumor tissue penetration. GOD catalyzes glucose (Glu) oxidation, inducing tumor starvation, while the resulting H_2O_2 triggers CO release, suppressing heat shock protein (HSP) expression and enhancing mild photothermal therapy (PTT). Mn^{2+} from MnCO initiates a Fenton-like reaction,

increasing intracellular ROS levels, while diselenide depletes glutathione (GSH), amplifying chemodynamic therapy (CDT). *In vitro* and *in vivo* experiments show that DSACGM NPs induce cancer cell apoptosis under NIR-II irradiation and efficiently ablate tumors in mice at sub-hyperthermic temperatures (<45°C) with excellent biocompatibility. This study provides valuable insights into nanomedicine design and its potential in advanced tumor therapies.

1. Introduction

The high global incidence and mortality rates of cancer result in nearly ten million deaths annually, presenting a paramount challenge to public health[1–3]. Developing safe and efficacious treatment strategies to address these diseases constitutes an urgent imperative and a primary focus of contemporary biomedical research. In clinical settings, conventional therapeutic modalities such as surgery, chemotherapy, and radiation therapy encounter limitations imposed by the intricate tumor microenvironment and frequently manifest severe adverse effects[4–6]. Consequently, researchers have innovated a diverse array of therapeutic interventions to circumvent these challenges. For example, near-infrared (NIR) light-based photothermal therapy (PTT) offers a promising approach for localized tumor ablation through controlled heating, characterized by its ease of manipulation and favorable biocompatibility[7,8]. The interest in NIR light within the near-infrared-II window (1000-1350 nm) is particularly noteworthy due to its superior tissue penetration depth[9]. However, applying high-temperature PTT raises concerns regarding collateral damage to adjacent healthy tissues and the elicitation of systemic immune responses[10,11]. Low-temperature PTT strategies (38-45°C) have been developed to mitigate these potential adverse effects[10,12]. Nevertheless, the induction of heat shock protein (HSP) expression as a consequence of heat stimulation compromises the therapeutic efficacy of low-temperature PTT by promoting the repair of thermally damaged cells[13,14]. Consequently, there is a pressing need to downregulate HSP expression to optimize the ablative potential of low-temperature PTT against tumors[15]. Chemodynamic therapy (CDT) disrupts the redox equilibrium within tumor cells, inducing sustained oxidative stress and ultimately culminating in apoptosis[16,17]. CDT typically elicits oxidative stress within cells through two pathways: (1) augmentation of reactive oxygen species levels within tumor cells. For example, through the Fenton reaction involving iron, copper, and manganese ions, hydrogen peroxide (H_2O_2) is converted into more potent hydroxyl radicals (·OH)[18–20]; (2) reduction of reducing agent levels. For instance, diselenide compounds effectively convert glutathione (GSH) to its oxidized form (GSSG), thereby diminishing GSH levels[21]. However,

monotherapy often yields suboptimal outcomes; thus, amalgamating diverse treatment modalities emerges as a promising therapeutic strategy.

The emergence of nanomaterials has unlocked promising avenues for advancing multi-modal therapeutic strategies[22,23]. Notably, Metal-Organic Frameworks (MOFs) stand out due to their porous morphology and structure-function tunability, rendering them versatile platforms for nanoscale integration[24–28]. For instance, Fang et al. synthesized nanoscale ferrocene MOF and encapsulated glucose oxidase (GOD), fabricating a cascade enzyme/Fenton catalysis therapeutic platform[29]. The enzymatic conversion of hydrogen peroxide by GOD augments the generation of ·OH via the Fenton reaction, thereby potentiating the therapeutic efficacy of CDT. Furthermore, the concomitant depletion of glucose (Glu) achieves a synergistic starvation therapy effect. Additionally, Liu et al. encapsulated a photosensitizer (Ce6) and a metabolic modulator (Lonidamine) within Zeolitic Imidazolate Framework-8 (ZIF-8), subsequently surface-modifying the construct with homologous tumor cell membranes[30]. This intervention enhances nanomaterial accumulation at tumor sites and synergistically eradicates tumors through the combined effects of photodynamic therapy (PDT) and immunotherapy. Despite showcasing distinct advantages in tumor treatment, the dense extracellular matrix and abnormally high tumor interstitial pressure at tumor sites hinder the deep diffusion of nanoparticles, thereby attenuating the therapeutic potency of nanomaterials[31–33].

In recent years, the rapid advancement of nanomotors has forged novel pathways for the deep tissue infiltration of nanomaterials into tumors and their intracellular penetration[34–39]. Nanomotors exhibit the capability to convert diverse energy sources into propulsive forces, encompassing external stimuli such as light, ultrasound, magnetic fields, electric fields[40–43], as well as internal chemical fuels like Glu, urea, and H_2O_2[44–46]. Particularly noteworthy are the NIR-II light-driven self-thermophoresis nanomotors, characterized by their precise spatiotemporal control and remarkable tissue penetration depths, facilitating tumor ablation through NIR-II-mediated PTT[47]. Additionally, nanomotors propelled by gases such as O_2 and NO can perform tumor penetration, and their released gases can assist in tumor treatment[48,49]. Currently, most nanomotor-based tumor therapies rely on single driving forces[48, 50–54]. We anticipate that the synergistic utilization of multiple propulsion mechanisms will significantly enhance the tumor penetration capacity of nanomotors. Therefore, developing multi-driven nanomotors for combined tumor therapy would be a promising oncological treatment strategy.

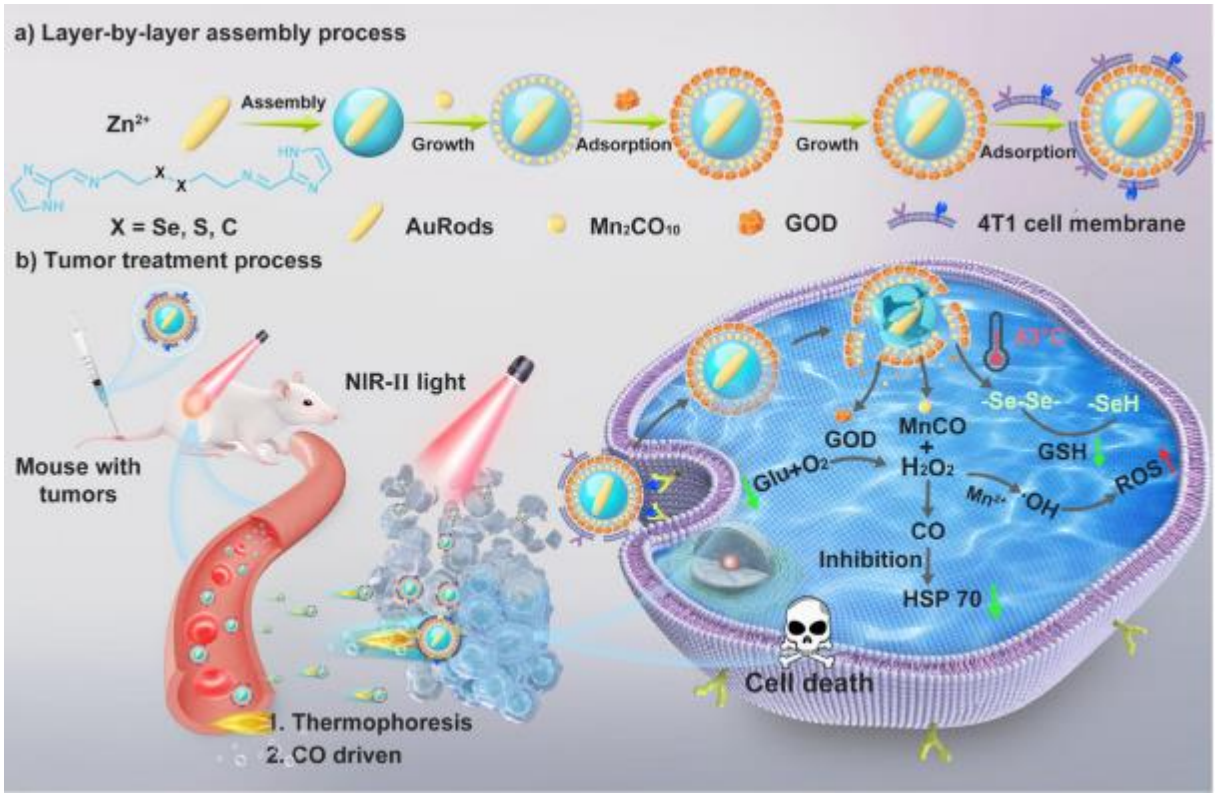

Scheme 1: Schematic illustration: a) Stepwise preparation route of the dual-driven nanomotor via layer-by-layer assembly; b) Penetration of DSACGM NPs into tumor tissue driven by NIR-II and CO, facilitating multimodal synergistic therapy, including starvation therapy, CDT, and mild PTT.

Drawing upon the preceding deliberations, we have devised a method to integrate gold nanorods with NIR-II absorption, Mn_2CO_{10} (MnCO), and GOD into a diselenium-containing MOF via a layer-by-layer assembly approach (Scheme 1a). Concurrently, fragments of tumor cell membranes were loaded onto the MOF's outermost layer to fabricate tumor-targeting dual-driven nanomotors (DSACGM NPs). This design aims to synergistically address tumor therapy through mild PTT, starvation therapy, and CDT. The MOF's encapsulation of tumor cell membranes endows the nanomotors with directional guidance toward tumor tissue. Under NIR-II irradiation, gold nanorods induce self-thermophoresis of the nanoparticles, serving as the primary driving force. Simultaneously, GOD catalyzes Glu to generate H_2O_2, subsequently oxidizing MnCO and releasing CO to propel nanoparticle movement, constituting the secondary driving force. The synergistic action of these dual driving forces facilitates nanoparticle aggregation and penetration into the tumor site. During irradiation, stringent control of light power density and exposure time (1 W/cm², 3 min) maintains

temperatures below 45°C. Moreover, CO release effectively mitigates the expression of HSP-70, ensuring efficient low-temperature PTT[55]. Continuous Glu consumption by GOD induces tumor cell starvation and elevates intracellular H_2O_2 levels. Additionally, the nanomaterials respond to the tumor's mildly acidic milieu to release diselenium molecules, which deplete intracellular antioxidant GSH in tumor cells. Furthermore, under weakly acidic conditions, H_2O_2 reacts with
MnCO, releasing Mn^{2+}, which triggers the Fenton-like reaction, generating highly toxic ·OH. The oxidative stress caused by CDT can be effectively amplified by the depletion of reduced substances and the increase of ROS levels to induce apoptosis (Scheme 1b). This study endeavors to enhance the tumor-penetrating capabilities of nanotherapeutic platforms via dual-driven nanomotor design. Furthermore, by integrating mild PTT, starvation therapy, and CDT in concert, synergistic eradication of cancer cells is achieved, offering valuable insights for nanomedicine design.

2. Results and Discussion

2.1. Synthesis and Characterization of dual-driven nanomotors

The dual-drive nanomotor was synthesized using a layer-by-layer assembly technique, sequentially encapsulating each component within a diselenide-containing MOF to ensure the effective performance of all components. We initially synthesized an imidazole derivative containing diselenide (compound 3) as the organic ligand and validated its structure using ^{1}H-NMR, ESI, and ^{77}Se-NMR (see Supporting Information). Compound 3 and zinc nitrate hexahydrate ($Zn(NO_3)_2·6H_2O$) were added to ultrapure water in a 2:1 molar ratio and vigorously stirred to synthesize a diselenide-containing MOF via a one-pot method (DSe NPs). Under an optical microscope, the synthesized diselenide MOF appeared uniformly dispersed small dots (Figure S13). Transmission electron microscopy (TEM), tapping-mode atomic force microscopy (AFM), and scanning electron microscopic (SEM) images further revealed that the diselenide MOF had a hollow spherical structure with a size of approximately 150 nm (Figure 1a, b, l and Figure S14). The hollow structure and size of the diselenide MOF facilitate the encapsulation of other components and are advantageous for biological applications. A solution of $Zn(NO_3)_2·6H_2O$ was added dropwise to a mixture containing compound 3 and cetyltrimethylammonium bromide (CTAB)-capped gold nanorods (AuNRs). After a 24-hour reaction period, diselenide MOF-coated AuNRs (DSA NPs) were obtained. TEM images revealed that the DSA NPs exhibited a well-defined core-shell structure and good dispersibility (Figure 1c, d), with an average size comparable to that of the DSe NPs (Figure 1l). The

synthesized DSA NPs were dispersed in a methanol solution, to which methanol-dissolved MnCO and compound 3 were subsequently added. After thorough mixing, a methanol solution

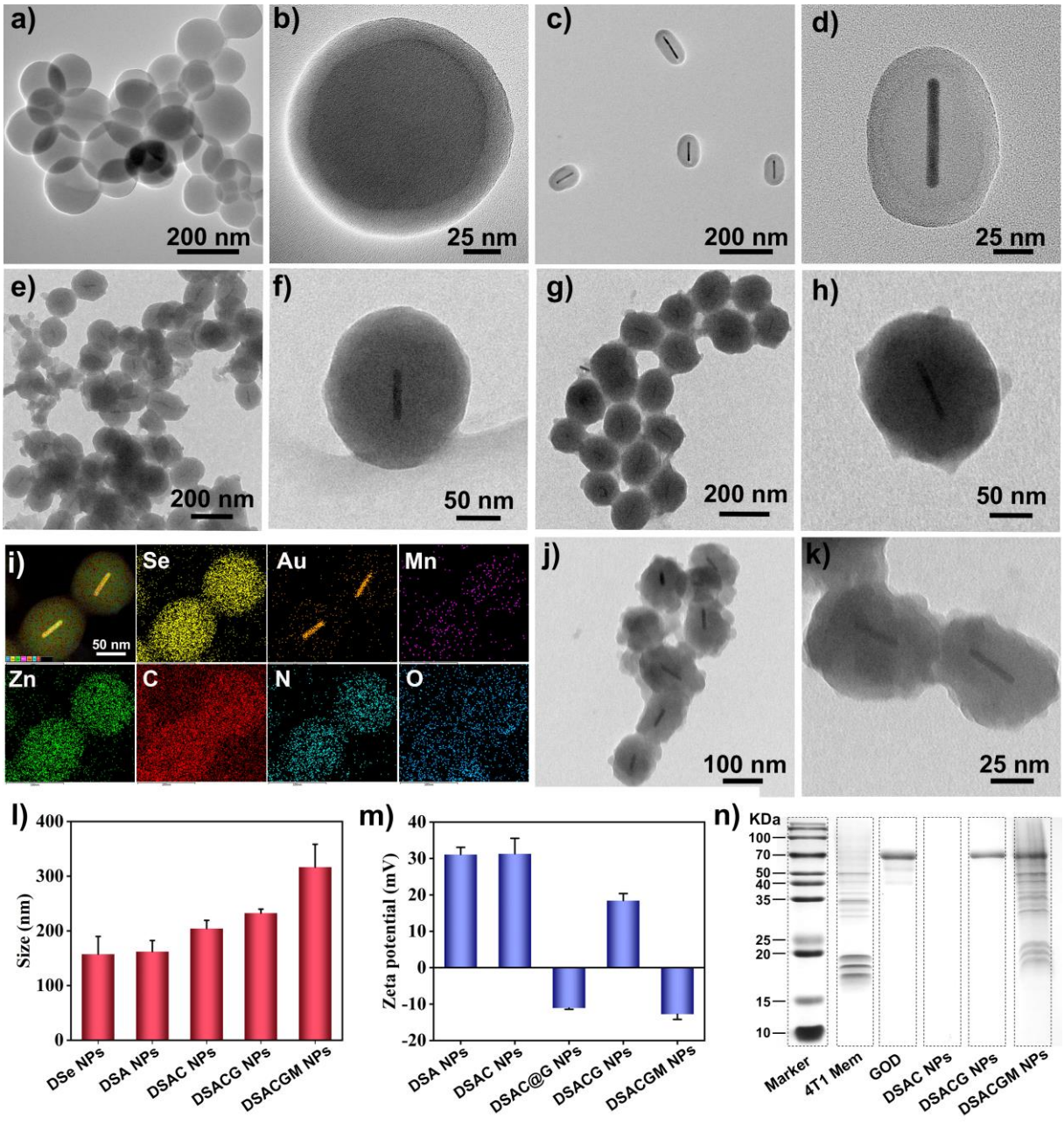

Figure 1: TEM images of a) and b) DSe NPs, c) and d) DSA NPs, e) and f) DSAC NPs, g) and h) DSACG NPs, i) and j) DSACGM NPs; k) HR-TEM and corresponding EDX elemental mappings of DSAC NPs; l) hydrodynamic size of DSe NPs, DSA NPs, DSAC NPs, DSACG NPs and DSACGM NPs; m) ζ-Potentials of DSA NPs, DSAC NPs, DSAC@G NPs, DSACG NPs, DSACGM NPs; n) SDS-PAGE analysis of 4T1 membrane, GOD, DSAC NPs, DSACG NPs and DSACGM NPs.

of $Zn(NO_3)_2 \cdot 6H_2O$ was added dropwise. Following the reaction, the resulting nanoparticles were thoroughly washed and redispersed in PBS solution, yielding diselenide MOFs coated with AuRods and MnCO (DSAC NPs). The concentration of MnCO was determined by UV

absorption (Figure S15, S16), indicating an encapsulation efficiency of 35.8% (Figure S17). TEM images revealed that the DSAC NPs retained the original core-shell structure (Figure 1e, f), with an increased average size compared to the DSA NPs (Figure 1l). This was attributed to the epitaxial growth characteristic of the isomorphic MOF[56,57], resulting in an additional MnCO-containing MOF shell. Elemental mapping images confirmed that the Au signal was centered. In contrast, Se, Zn, C, and N signals were uniformly distributed throughout, and Mn and O signals were primarily concentrated on the outer layer (Figure 1i).

The GOD encapsulation process occurred in two sequential steps. Initially, GOD was mixed with an aqueous solution of DSAC NPs. Due to GOD's isoelectric point at 4.2, it carries a negative charge in water, while DSAC NPs possess a positive charge (Figure 1m). Consequently, electrostatic interactions facilitated the adsorption of GOD onto the outer surface of DSAC NPs, yielding negatively charged nanoparticles (DSAC@G NPs) (Figure 1m). Subsequently, the addition of compound 3 and $Zn(NO_3)_2 \cdot 6H_2O$ to the DSAC@G NPs solution resulted in the formation of diselenide MOF nanoparticles coated with AuRods, MnCO, and GOD (DSACG NPs). TEM imaging confirmed the core-shell structure of DSACG NPs (Figure 1g, h), with a slightly larger average particle size than DSAC NPs and exhibiting a positively charged surface (Figure 1l, m). Rhodamine B-modified GOD was employed to quantify the encapsulation efficiency of GOD, and fluorescence-based quantification revealed a coverage rate of 98.4% (Figure S18, S19). Additionally, centrifugation of the solution indicated minimal fluorescence in the supernatant, suggesting the majority of Rhodamine B-modified GOD was concentrated in the precipitate at the bottom (Figure S20). Furthermore, SDS-PAGE analysis provided further confirmation of successful GOD encapsulation (Figure 1n). In addition, since GOD can catalyze the production of H_2O_2 from Glu, H_2O_2 can further react with MnCO to produce CO. The introduction of Glu solutions with MnCO, DSAC NPs, and DSACG NPs separately, followed by the detection of CO generation using gas chromatography, demonstrated that only the DSACG group exhibited CO production, indirectly confirming successful GOD loading (Figure S21). The coating of cell membranes enhances the targeting capability of nanoparticles to homologous tumors[58]. Therefore, we loaded 4T1 cell membrane fragments onto the surface of DSACG NPs using sonication. This process resulted in DSACGM NPs with a roughened surface (Figure 1j, k) and negative surface potential (Figure 1m). SDS-PAGE analysis further confirmed the successful incorporation of the cell membranes (Figure 1n).

2.2. Performance evaluation

2.2.1. Evaluation of photothermal properties

AuRods exhibit transverse and longitudinal plasmonic resonance bands at 513 and 1095 nm, respectively (Figure 2a). The increased dielectric constant of the diselenide MOF shell in the synthesized DSACGM NPs induced a redshift in the longitudinal plasmonic resonance (Figure 2a), a phenomenon corroborated by previous studies[59,60]. To investigate the *in vitro* photothermal properties of DSACGM NPs, we employed a thermal imaging camera to monitor temperature elevation induced by NIR laser irradiation and recorded the temperature variations over time. Using PBS solution as a control, DSACGM NPs solutions at various concentrations (100, 200, 500, 1000 μg/mL) were irradiated with an NIR-II laser (1064 nm, 1.0 W/cm²) for 12 minutes. As illustrated in Figure 2c, the average temperature of the DSACGM NPs solutions increased with irradiation time, with higher DSACGM NPs concentrations resulting in faster heating rates and higher equilibrium temperatures. Furthermore, DSACGM NPs solutions (500 μg/mL) were irradiated with NIR-II light at different power densities (0.2, 0.5, 1.0, 1.5 W/cm²), and the temperature changes were monitored. As depicted in Figure 2d, the photothermal effect of DSACGM NPs demonstrated a power density dependence, with higher power densities yielding faster heating rates and higher equilibrium temperatures. Additionally, DSACGM NPs exhibited remarkable photothermal conversion cycle stability, maintaining significant photothermal effects after five heating/cooling cycles, with no noticeable change in the maximum temperature (Figure 3e). Using the cooling curve of the DSACGM NPs solution (500 μg/mL) post NIR-II irradiation at 1.0 W/cm², we obtained the linear fit of the negative natural logarithm of temperature versus cooling time (Figure 2f), calculating a photothermal conversion efficiency of 48.2%. These findings suggest that DSACGM NPs possess significant PTT potential.

2.2.2. Evaluation of CO release capacity

Oxidizing agents such as H_2O_2 and ·OH can degrade MnCO, leading to the release of CO. Initially, we validated the CO release capacity of DSACGM NPs *in vitro*, utilizing hemoglobin as a probe for CO detection (Figure 2g). As illustrated in Figure 2h, oxyhemoglobin (Hb-O_2), deoxyhemoglobin (Hb), and carboxyhemoglobin (Hb-CO) exhibit distinct characteristic absorption peaks, enabling the quantification of CO release through these spectral differences. To derive the formula for calculating CO release, we measured the UV absorption spectra of varying concentrations of Hb and Hb-CO to determine the requisite molar extinction coefficients (Figure 2i). Subsequently, using H_2O_2 as an inducer, we evaluated the CO release from DSACGM NPs at different concentrations (40, 60, 80, 120, 200 μg/mL). As shown in

Figure 2j, with increasing concentrations of DSACGM NPs, the characteristic absorption peak of Hb at 430 nm progressively decreased, while the absorbance of Hb-CO at 420 nm increased, indicating enhanced CO release. At a DSACGM NPs concentration of 200 μg/mL, the CO release was approximately 1.14 μM (Table S1), thus confirming the CO release capability of the DSACGM NPs.

2.2.3 Evaluation of GOD Activity

Encapsulation of enzymes within MOFs can result in a degree of activity reduction, potentially due to alterations in enzyme conformation or interference with the active site[61]. Therefore, it is imperative to ascertain the activity of GOD encapsulated within DSACGM NPs to ensure its functionality in biological applications. The catalytic oxidation of Glu by GOD is an oxygen-consuming process. Thus, a dissolved oxygen meter was employed to monitor changes in oxygen concentration in the Glu solution to evaluate GOD activity. As depicted in Figure 2l, the dissolved oxygen levels in the Glu solution containing GOD decreased significantly over time. Conversely, the rate of oxygen depletion was reduced in the Glu solution containing DSACGM NPs, indicating that the MOF shell impacts GOD activity. By recording the oxygen consumption rates of DSACGM NPs in Glu solutions of varying concentrations, we observed that the enzyme kinetics adhered to Michaelis-Menten dynamics (Figure 2m), demonstrating that GOD encapsulated within the MOF shell retained significant enzymatic characteristics. Utilizing Lineweaver-Burk plots (Figure 2n) and the Michaelis-Menten equation, we calculated the enzymatic constants associated with GOD (Table S2). The results indicated that the apparent Michaelis-Menten constant (*Km*) of DSACGM NPs was approximately half that of free GOD, likely due to the partial obstruction of the MOF shell hindering the interaction between GOD and its substrate, Glu. The maximum reaction rate (*Vmax*) of DSACGM NPs was approximately 58.7% of that of free GOD. Despite the reduction in GOD activity post-encapsulation, the apparent second-order rate constant (*kcat/Km*) remained within the same order of magnitude as that of free GOD, indicating that the enzyme retained most of its catalytic activity. Moreover, the MOF shell achieved a 98.7% encapsulation efficiency for GOD, suggesting that the reduction in GOD activity would not significantly affect its subsequent biological applications.

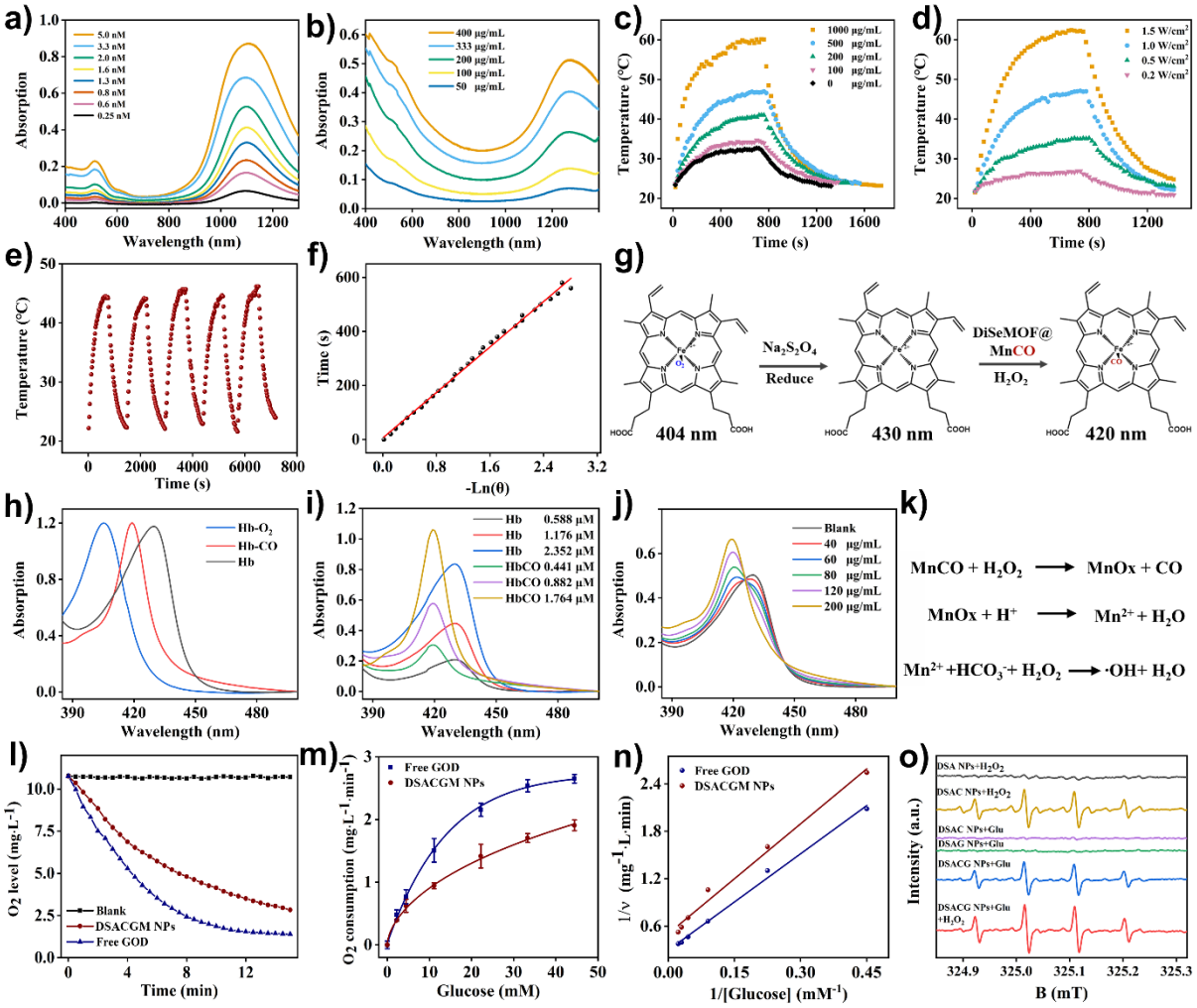

Figure 2: UV absorption of a) AuRods and b) DSACGM NPs; c) Temperature variation curves of different concentrations of DSACGM NPs during and after NIR-II irradiation; d) Temperature variation curves of DSACGM NPs (500 μg/mL) under NIR-II irradiation at different power densities; e) heating and cooling curves of DSACGM NPs irradiated by NIR-II laser over five ON/OFF cycles; f) the linear fit of the negative natural logarithm of temperature versus cooling time (DSACGM NPs); g) schematic illustration of the conversion between Hb-O_2,Hb and Hb-CO; h) UV absorption of Hb-O_2,Hb and Hb-CO; i) UV absorption of different concentrations of Hb and Hb-CO; j) changes in Hb UV absorption after CO release from DSACGM NPs at different concentrations; k) Equations for the reaction of H_2O_2 with MnCO to release CO and Mn^{2+} and for Mn^{2+}-induced Fenton-like reactions. l) O_2 consumption by free GOD and DSACGM NPs in Glu solution, controlling for a GOD concentration of 2 μg/mL. m) steady-state kinetic assay of free GOD and DSACGM NPs with Glu; n) Lineweaver-Burk plots of GOD activity of the free GOD and DSACGM NPs; o) EPR signal of •OH radical.

2.2.4 Detection of ·OH

In mildly acidic conditions, H^+ and H_2O_2 can efficiently convert MnCO into Mn^{2+} and CO[62]. In the presence of bicarbonate (HCO_3^-), the Mn^{2+}-mediated Fenton-like reaction can convert H_2O_2 into highly cytotoxic ·OH[63]. Given that HCO_3^-/CO_2 is a crucial physiological buffer, bicarbonate is abundantly present in biological systems. To detect ·OH radicals, 5,5-dimethyl-

1-pyrroline-N-oxide (DMPO) was employed as a radical scavenger, forming a DMPO/·OH adduct that exhibits a characteristic ESR signal with a quartet pattern of 1:2:2:1 intensity ratio. As illustrated in Figure 2o, DSAC NPs generated a significant ESR signal under conditions of pH=6.5, $NaHCO_3$ (25 mM), and H_2O_2 (1 mM), indicating the formation of ·OH. Substituting H_2O_2 with Glu resulted in a discernible ESR signal for DSACG NPs, suggesting that DSACG NPs can catalyze the production of H_2O_2 from Glu, thereby triggering the Fenton-like reaction. In the simultaneous presence of H_2O_2 and Glu, DSACG NPs exhibited an even stronger ESR signal, demonstrating that GOD encapsulated within DSACG NPs can enhance the generation of ·OH under physiological conditions.

2.2.5 Monitoring of intracellular ROS levels and CO release

In the study above, we have confirmed the catalytic activity of GOD encapsulated in DSACGM NPs and their proficiency in generating ·OH. Subsequently, we employed 2',7'-dichlorofluorescein diacetate (DCFH-DA) as a ROS probe to evaluate the ROS-generating capability of DSACGM NPs within 4T1 cells. As depicted in the CLSM images in Figure 3a, following an eight-hour incubation of DSACGM NPs with 4T1 cells, intracellular ROS levels showed a marked increase. Additionally, a concentration-dependent escalation in ROS levels was observed with increasing DSACGM NPs concentration. These findings demonstrate that DSACGM NPs can effectively augment intracellular ROS levels, facilitating subsequent tumor CDT. Furthermore, we quantified intracellular H_2O_2 levels in 4T1 cells using a hydrogen peroxide assay kit. The results indicated that, although a fraction of H_2O_2 reacts with MnCO to produce ·OH, the overall intracellular H_2O_2 levels remained elevated (Figure 3b). This persistent oxidative stress is conducive to inducing cellular apoptosis, enhancing the therapeutic efficacy.

To ascertain the capacity of DSACGM NPs for CO release within tumor cells, we synthesized a CO-specific probe (FL-CO-1) for intracellular CO detection. FL-CO-1 enables sensitive detection of CO in the presence of $PdCl_2$. As shown in Figure 3c, compared to the control group, the group treated with MnCO exhibited weak fluorescence, likely due to MnCO's poor solubility under physiological conditions, impeding its effective cellular uptake. Conversely, the group treated with DSACM NPs demonstrated significantly enhanced intracellular fluorescence intensity, indicating efficient delivery of MnCO into cells and subsequent CO release by the nanocarrier. The DSACGM NPs-treated group showed intense green fluorescence within 4T1 cells, attributed to GOD's role in elevating intracellular H_2O_2 levels, thereby facilitating CO release. These findings confirm that DSACGM NPs can effectively

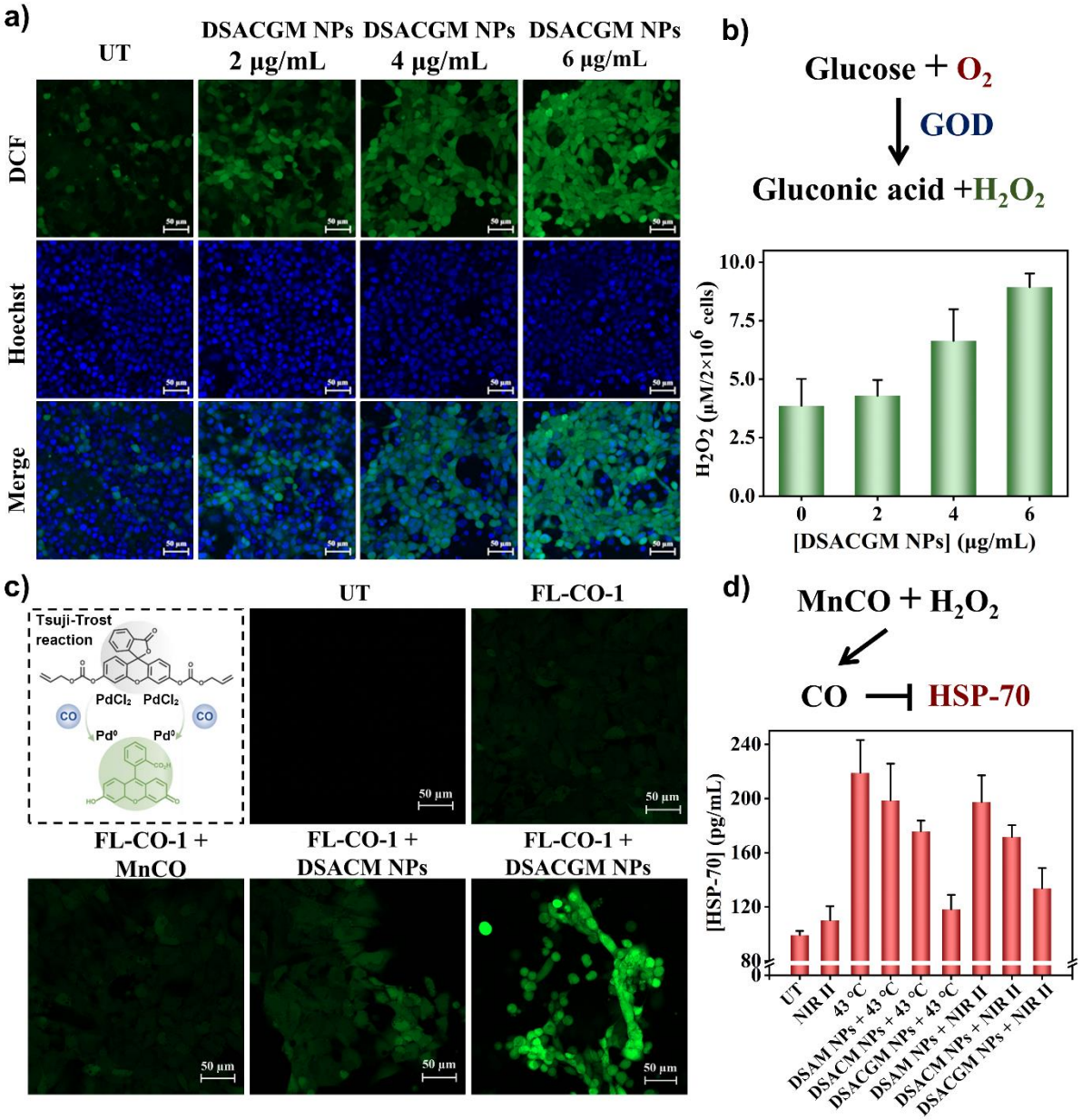

Figure 3: a) Representative images of the fluorescence of DCF of different concentrations of DSACGM NPs; b) Changes in H_2O_2 content after incubation of 4T1 cells with different concentrations of DSACGM NPs; c) intracellular CO detection: 4T1 cells subjected to various treatments were stained with the FL-CO-1 probe, followed by visualization and imaging using CLSM; d) Enzyme-linked immunosorbent assay (ELISA) results of HSP-70 content in 4T1 cells treated under different conditions.

release CO, owing to the elevated intracellular H_2O_2 levels and the production of ·OH via the Mn^{2+}-mediated Fenton-like reaction. CO release can suppress the expression of intracellular HSPs, enhancing the efficacy of mild PTT. We utilized an enzyme-linked immunosorbent assay (ELISA) to measure HSP-70 levels in cells following various treatments to validate this inhibitory effect (Figure 3d). At 43°C, DSACGM NPs treatment significantly inhibited the

overexpression of HSP-70 in 4T1 cells. Under NIR-II irradiation, DSACGM NPs also effectively reduced HSP-70 expression.

2.2.6 Motion analysis of DSACGM NPs

To determine the driving force of DSACGM NPs, we also prepared DSM NPs, DSCM NPs, DSGM NPs, and DSCGM NPs and investigated their motility under various conditions (PBS, Glu, NIR-II, and Glu+NIR-II). We meticulously tracked the trajectories of these nanomotors and conducted a comprehensive analysis, calculating the effective diffusion coefficients (Deff), instantaneous mean velocities (Speed), and mean squared displacements (MSD). As shown in Figure 4a, DSM NPs, DSCM NPs, and DSGM NPs exhibited isotropic Brownian motion across all tested conditions. In contrast, DSCGM NPs displayed prolonged trajectories exclusively in Glu-containing solutions, suggesting that H_2O_2 generated by the catalytic activity of GOD within DSCGM NPs induces CO release, thus propelling the nanoparticles. The calculated Deff values and fitted MSD curves corroborate the autonomous diffusion of DSCGM NPs in Glu solutions (Figure 4b, d, e, f and S24), with a corresponding increase in instantaneous mean velocity (Figure 4c). Under NIR-II irradiation, DSCGM NPs' motion trajectory remained largely unaltered, whereas DSACGM NPs demonstrated significant directional movement (Figure 4a). Under combined Glu+NIR-II conditions, DSACGM NPs exhibited enhanced autonomous motility, consistent with Deff (3.09 $\mu m^2/s$) and MSD curve analyses (Figure 4b, d). We hypothesize that this directed motion arises from the asymmetric structural configuration induced by random cell membrane adsorption. Furthermore, we evaluated DSACGM NPs' motility across varying Glu concentrations and NIR-II light power densities. Higher Glu concentrations resulted in more pronounced directional movement of DSACGM NPs (Figure S25). Additionally, DSACGM NPs exhibited power density-dependent motility behavior, likely due to augmented thermophoretic propulsion generated by higher NIR-II light intensities (Figure S26).

Subsequently, we synthesized RhB-labeled DSCGM NPs (RhB-DSCGM NPs) and employed confocal microscopy and flow cytometry to investigate the cellular uptake behavior of these nanomotors under various conditions. As depicted in Figure S27a, the nanomotors exhibited markedly enhanced cellular internalization in a high-Glu DMEM medium. Post-irradiation, 4T1 cells demonstrated intensified red fluorescence, indicating that the nanomotors, driven by gaseous and photothermal effects, can significantly enhance cellular penetration. Flow cytometry results corroborated these findings, showing the highest fluorescence intensity in 4T1 cells under high-Glu and NIR-II irradiation conditions (Figure S27b). To further explore

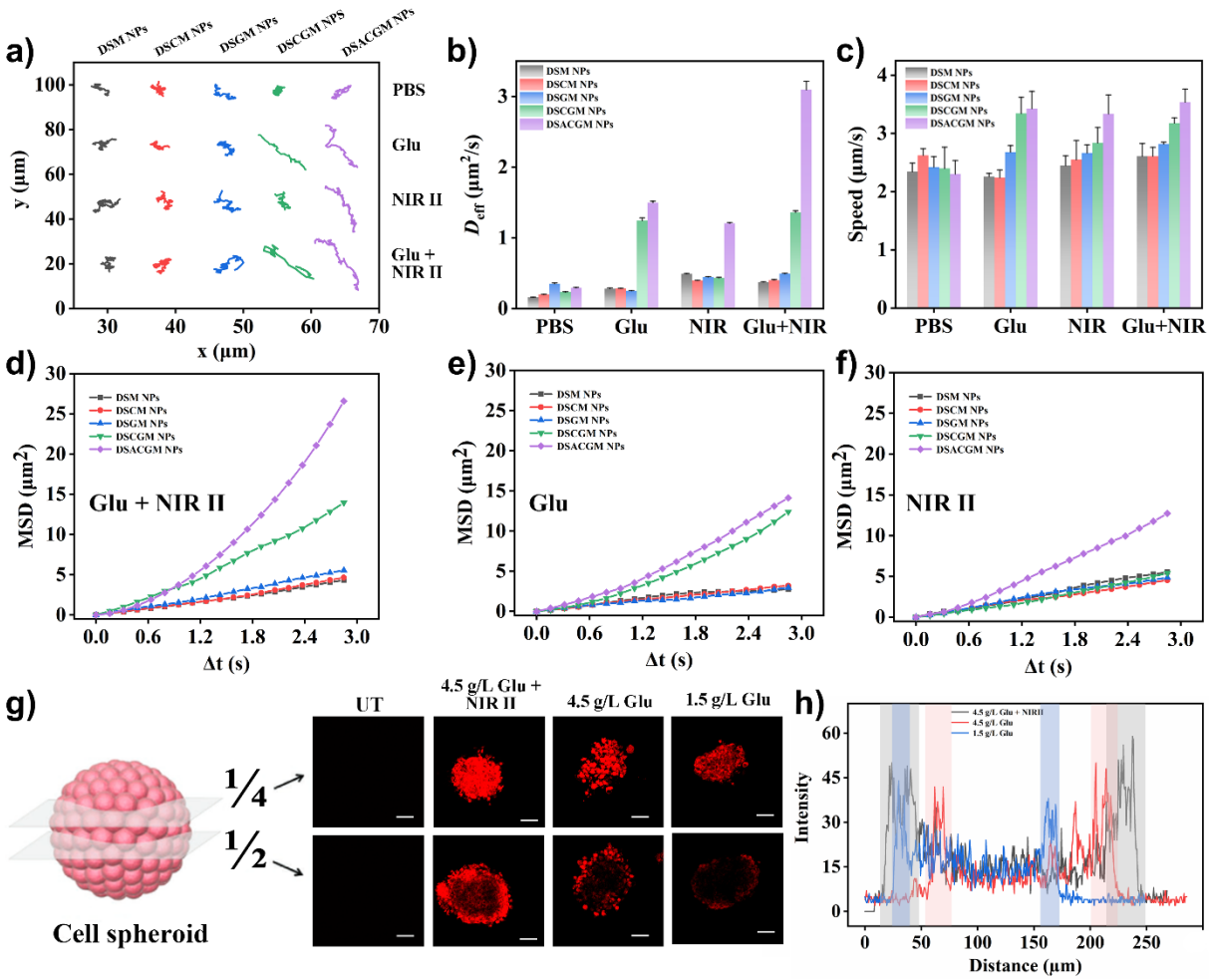

Figure 4: a) Representative tracking trajectories of DSM NPs, DSCM NPs, DSGM NPs, DSCGM NPs, and DSACGM NPs under different conditions; b) and c) the corresponding D_{eff} and speeds; d), e), f) average MSD versus time interval (Δt) analyzed from tracking trajectories; g) Penetration of DSACGM NPs into 3D MTS under various conditions via viaz-stack scanning. Scalebar, 50 μm. h) fluorescence intensity analysis along the symmetric axis of the 1/2 cross-section using ImageJ.

the permeability of the nanomotors, we constructed a 3D multicellular tumor spheroid (MTS) model. As illustrated in Figure 5g, under high-Glu and NIR-II irradiation conditions, RhB-DSCGM NPs achieved the maximal penetration depth (approximately 40 μm). The fluorescence spectra of the cross-section at half the depth of the 3D MTS indicated that gas propulsion induced by Glu and thermophoretic movement triggered by NIR significantly enhanced the penetration depth of the nanomotors (Figure 4h).

2.3. In Vitro Antitumor Efficacy

Diselenide bonds can effectively scavenge intracellular GSH in cancer cells, thereby diminishing cell viability and inducing apoptosis. To ascertain the cytotoxicity of diselenide MOFs, we synthesized imidazole derivatives linked by disulfide bonds and carbon chains. The

MOFs formed by the coordination of these compounds with Zn^{2+} were designated as Cys NPs and Hes NPs, respectively (Figure S28). FITC was encapsulated within the DSe NPs, and TEM and SEM images demonstrated that the FITC-loaded DSe NPs retained their spherical morphology (Figure S29). CLSM results confirmed that DSM NPs could internalize within 4T1 cells (Figure S29). As depicted in Figure 5a, DSM NPs exhibited significantly more cytotoxicity than CysM NPs and HesM NPs. Furthermore, cells treated with DSM NPs showed a substantial reduction in GSH levels by approximately 50% (Figure S30), and the GSH depletion capability of DSM NPs exhibited a concentration-dependent response (Figure S30).

To confirm the targeting specificity of DSACGM NPs toward 4T1 cells, we incubated RhB-DSCGM NPs with various cell lines (B16, HL, NRK, PC12, 769-P, A549, and 4T1) and utilized flow cytometry to quantify intracellular fluorescence intensity. The results revealed that fluorescence intensity was significantly elevated in 4T1 cells (Figure S31). Furthermore, DSACGM NPs exhibited pronounced cytotoxicity against 4T1 cells (Figure 5b).

To validate the cascade therapeutic efficacy of DSACGM NPs, we also synthesized DSAM NPs, DSACM NPs, and DSAGM NPs. Cytotoxicity assays revealed that DSACGM NPs exhibited significantly greater cytotoxicity compared to the other synthesized nanomaterials (Figure 5c), accompanied by a marked reduction in intracellular Glu levels (Figure S32). Under NIR-II irradiation (1 W/cm², 3 min) while maintaining the temperature below 45°C, 2 μg/mL of DSACGM NPs nearly eradicated all 4T1 cells (Figure 5c). The apoptosis-inducing capability of DSACGM NPs demonstrated a concentration-dependent response (Figure S33). As depicted in Figure 5d, NIR-II irradiation alone did not induce apoptosis in 4T1 cells. Cells treated with DSAM NPs, DSACM NPs, DSAGM NPs, DSACGM NPs, and DSACGM NPs+NIR-II exhibited 32.2%, 58.3%, 66.3%, 81.0%, and 91.3% late apoptosis, respectively, substantiating the synergistic cytotoxic efficacy of the nanocomposite components. Live/dead cell assays corroborated these findings (Figure 5f). Specifically, the diselenide components in DSACGM NPs effectively reduce intracellular GSH levels, while GOD elevates intracellular H_2O_2 levels and concurrently decreases Glu levels. The generated H_2O_2 further induces MnCO to release CO and Mn^{2+}. CO inhibits the expression of HSP, thereby enhancing the efficacy of mild PTT, while Mn^{2+} induces a Fenton-like reaction, producing highly $OH\cdot$. This synergistic mechanism combines starvation therapy, CDT, and PTT. JC-1 assays indicated that 96.3% of 4T1 cells treated with DSACGM NPs+NIR-II exhibited a decrease in mitochondrial membrane potential. CLSM images also demonstrated that JC-1 in cells treated with DSACGM NPs+NIR-II predominantly remained in the monomeric state, emitting strong green fluorescence (Figure

S34). These results indicate that DSACGM NPs effectively induce apoptosis, supporting further *in vivo* experimentation.

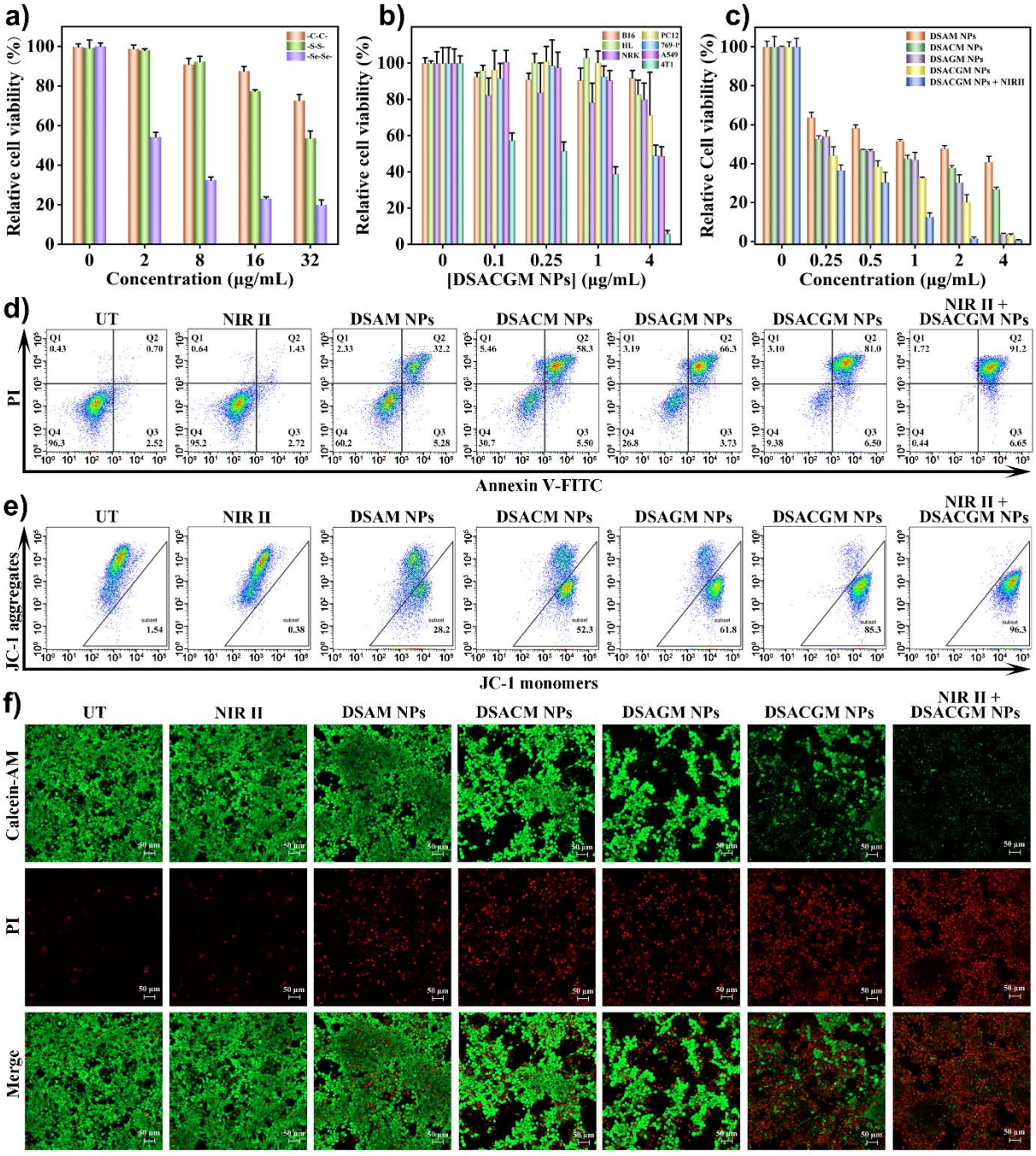

Figure 5: a) Cytotoxicity of DSM NPs (purple), CysM NPs and (green) and HesM NPs (orange) by CCK-8 analysis at different concentrations; b) Cytotoxicity of DSACGM NPs across various cell lines (B16, HL, NRK, PC12, 769-P, A549, 4T1); c) Cytotoxicity of DSAM NPs, DSACM NPs, DSAGM NPs , DSACGM NPs and DSACGM NPs + NIR-II by CCK-8 analysis at different concentrations; flow analysis results of d) Annexin V-FITC/PI or e) JC-1 stained apoptotic cells treated with different conditions; f) CLSM images of 4T1 cells after treated with various disposes. The cells were stained by calcein-AM/PI before the analysis by CLSM.

2.4. *In Vivo* Antitumor Efficacy

To evaluate the antitumor efficacy of DSACGM NPs, we constructed a 4T1 tumor-bearing mouse model. The extremely low hemolysis rate of DSACGM NPs preliminarily validated their biocompatibility (Figure S35). Cy5.5-labeled DSACG NPs and DSACGM NPs were synthesized to elucidate the temporal biodistribution. Figure 6a illustrates the fluorescence intensity of the tumor over time. The fluorescence signal at the tumor site reached its zenith 10 hours post-tail vein injection of DSACGM NPs, indicating maximal nanoparticle accumulation and establishing the optimal time point for NIR-II irradiation (Figure 6b). Compared to DSACG NPs, DSACGM NPs also exhibited an extended fluorescence decay time, indicating prolonged systemic circulation (Figure 6b). 24 hours post intravenous administration, tumors, and major organs were harvested from euthanized mice for ex vivo fluorescence imaging. The results revealed higher fluorescence intensity in tumors treated with DSACGM NPs than those treated with DSACG NPs (Figure 6c). Notably, the fluorescence in the liver and kidneys was higher than in other organs (Figure 6c), likely due to the metabolic processing of the nanoparticles by these organs.

4T1 tumor-bearing mice were divided into seven groups to evaluate the antitumor efficacy and subjected to various treatments. PBS or nanoparticles were administered intravenously at bi-daily intervals for a total of five injections. The mice were sacrificed and analyzed 14 days post-treatment. Initially, we monitored the temperature variation of the tumor surface under NIR-II irradiation (1.0 W/cm², 3 min). As depicted in Figure S36, the tumor temperature in the DSACGM NPs-treated mice stabilized around 44°C, facilitating mild photothermal therapy (PTT). In contrast, the PBS group exhibited tumor temperatures of approximately 40°C. This temperature differential is attributed to the accumulation of DSACGM NPs at the tumor site.

Comparative analyses of tumor volume, average size, and weight demonstrated significant tumor suppression in all treatment groups relative to the PBS and NIR-II groups (Figure 6d, f, g). Notably, the DSACGM NPs + NIR-II cohort exhibited superior antitumor efficacy, owing to the effective accumulation of nanomotors at the tumor locus and the synergistic multimodal therapeutic approach (encompassing starvation therapy, CDT, and mild PTT). Histopathological evaluation via H&E and TUNEL staining of tumor sections revealed that the DSACGM NPs + NIR-II group induced the highest apoptotic rates (Figure 6h), concomitant with significant reductions in intracellular GSH and Glu levels (Figure S37). Immunofluorescence staining for HSPs showed a moderate increase in red fluorescence post-NIR-II irradiation; however, marked reductions were observed in the DSACM NPs, DSACG

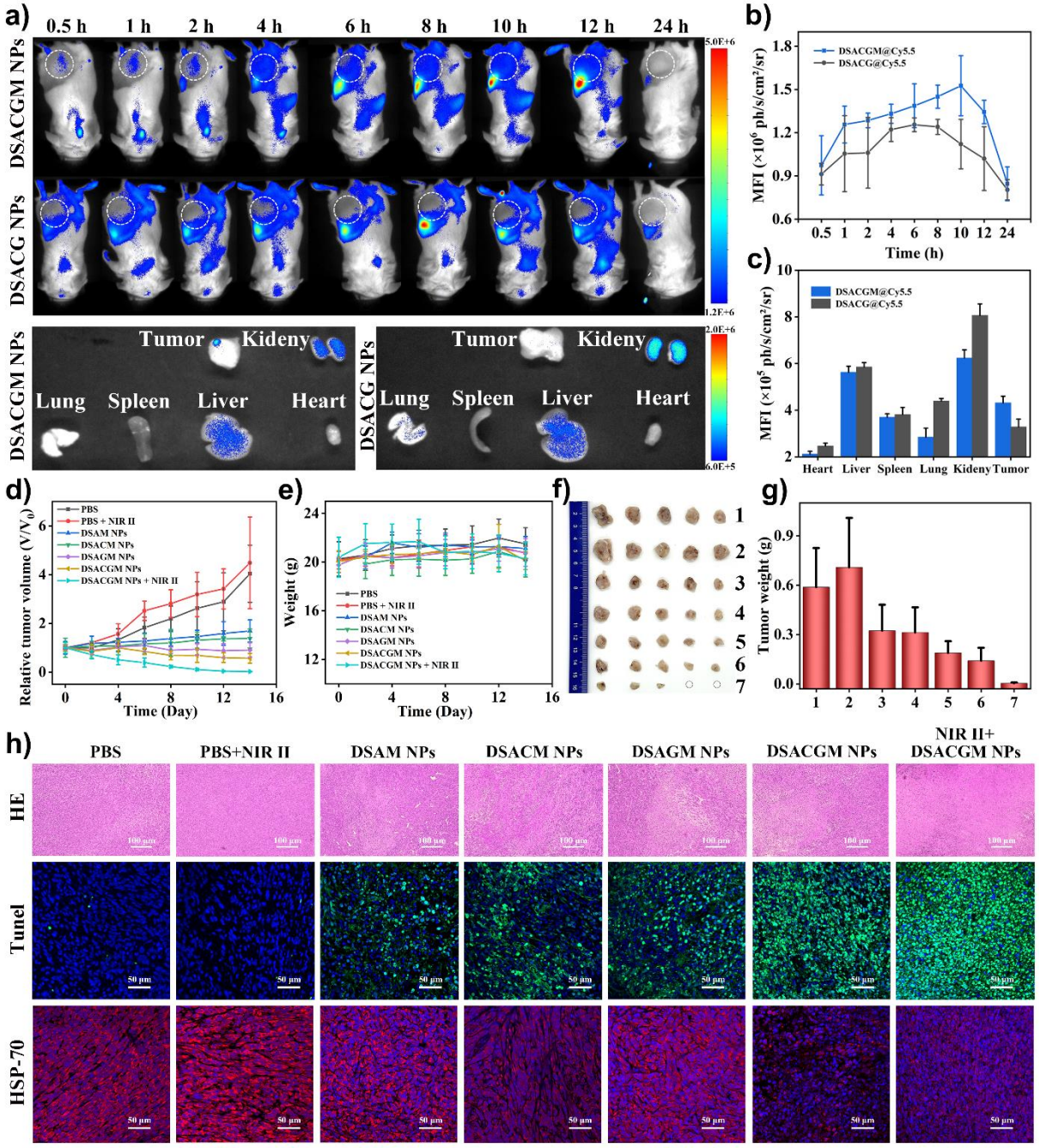

Figure 6: a) *In vivo* fluorescence imaging at various time points and b) corresponding MFI values following intravenous injection of Cy5.5@DSACGM NPs and Cy5.5@DSACG NPs in 4T1 tumor-bearing mice. a) *Ex vivo* fluorescence imaging of tissues 24 hours post-injection and (c) corresponding tissue MFI values. d) d) Changes in relative tumor volume across different groups; e) variations in body weight of 4T1 tumor-bearing mice across different groups during the experimental period; f) *Ex vivo* images of tumors from different groups after 14 days of treatment and g) corresponding *ex vivo* tumor weights; h) H&E, TUNEL, and HSP-70 immunofluorescence staining results of tumor tissues after 14 days of treatment. (1: PBS group, 2: PBS + NIR-II group, 3: DSAM NPs group, 4: DSACM NPs group, 5: DSAGM NPs group, 6: DSACGM NPs group, 7: DSACGM NPs + NIR-II group)

Each group of mice was weighed at two-day intervals to assess the *in vivo* biocompatibility of the nanoparticles, and only minimal variations in body weight were observed (Figure 6e).

NPs, and DSACGM NPs + NIR-II groups, indicative of suppressed HSP expression (Figure 6h).

Furthermore, histopathological analysis via H&E staining of major organs indicated no discernible tissue damage or inflammatory responses across all experimental groups (Figure S38). These findings substantiate the negligible toxicity and high biocompatibility of the nanomaterials.

3. Conclusion

In summary, we developed a dual-driven nanomotor based on diselenium MOFs through a layer-by-layer assembly technique for multimodal synergistic oncotherapy. The nanomotor is functionalized with a cancer cell membrane, which provides direction for the nanomotors to drive toward the tumor site. The release of CO and the photothermal effects of AuRods effectively propel the nanomotors, enhancing their tumor-specific accumulation. The encapsulated GOD depletes glucose, inducing starvation therapy, while the resultant H_2O_2 release triggers CO liberation, inhibits HSP expression, and augments mild PTT. The Mn^{2+} released from MnCO catalyzes a Fenton-like reaction, increasing intracellular ROS levels, whereas the diselenium component diminishes antioxidant GSH levels, thus potentiating CDT. *In vitro* and *in vivo* studies demonstrated that under NIR-II irradiation, DSACGM NPs effectively induced apoptosis, reduced mitochondrial membrane potential, and efficiently ablated tumors in murine models at sub-lethal temperatures (<45°C) while exhibiting excellent biocompatibility. Collectively, our findings provide significant insights into the design of advanced nanomotors and their application in targeted multimodal cancer therapy.

4. Experimental Section

Preparation of DiSeMOF NPs (DSe NPs): Typically, 60 mg of compound 3 was dispersed in 30 mL of ultrapure water with vigorous stirring at room temperature. 24.3 mg of zinc nitrate hexahydrate was dissolved in 1 mL of ultrapure water, slowly adding dropwise to the above solution. After the dropwise addition, the stirring was continued at room temperature for 24 hours. Subsequently, the reacted solution was fully centrifuged (14 000 g, 10 min), and the collected precipitate was washed three times with ultrapure water. Finally, the residue obtained was dispersed in a PBS solution for subsequent use.

Preparation of CysMOF NPs (Cys NPs): Typically, 46 mg of compound 4 was dispersed in 30 mL of ultrapure water with vigorous stirring at room temperature. 24.3 mg of zinc nitrate hexahydrate was dissolved in 1 mL of ultrapure water, slowly adding dropwise to the above

solution. After the dropwise addition, the stirring was continued at room temperature for 24 hours. Subsequently, the reacted solution was fully centrifuged (14 000 g, 10 min), and the collected precipitate was washed three times with ultrapure water. Finally, the residue obtained was dispersed in a PBS solution for subsequent use.

Preparation of HesMOF NPs (Hes NPs): Typically, 40 mg of compound 5 was dispersed in 30 mL of ultrapure water with vigorous stirring at room temperature. 24.3 mg of zinc nitrate hexahydrate was dissolved in 1 mL of ultrapure water, slowly adding dropwise to the above solution. After the dropwise addition, the stirring was continued at room temperature for 24 hours. Subsequently, the reacted solution was fully centrifuged (14 000 g, 10 min), and the collected precipitate was washed three times with ultrapure water. Finally, the residue obtained was dispersed in a PBS solution for subsequent use.

Preparation of DiSe@AuRod NPs (DSA NPs): Typically, 2 mg of compound 3 was dispersed in 2 mL of ultrapure water with vigorous stirring at room temperature. 0.5 mL of the gold rod solution was taken, centrifuged (14 000 g, 10 min), and washed twice with ultrapure water, which was subsequently added to the solution containing compound 3. Another 0.81 mg of zinc nitrate hexahydrate was dissolved in 50 μL of ultrapure water, and it was slowly added dropwise to the above-mixed solution. After the dropwise addition, it was continued at room temperature under stirring for 24 hours. Subsequently, the reacted solution was fully centrifuged (14 000 g, 10 min), and the collected precipitate was washed three times with ultrapure water. Finally, the precipitate obtained was dispersed in PBS solution also for subsequent use.

Preparation of DiSe@AuRod@MnCO NPs (DSAC NPs): Typically, 1 mL of DSA NPs solution was centrifuged, and the resulting precipitate was redispersed in methanol to which 2 mg of compound 3. 5 mg of Mn_2CO_{10} was taken dissolved in methanol and added to the methanol solution of DSA NPs with vigorous stirring. Another 0.81 mg of zinc nitrate hexahydrate was dissolved in 50 μL of ultrapure water, which was slowly added dropwise to the above-mixed solution. After the dropwise addition, it was continued at room temperature under stirring for 24 hours. Subsequently, the reacted solution was fully centrifuged (14 000 g, 10 min), and the collected precipitate was washed three times with methanol. Finally, the obtained residue was dispersed in PBS and prepared for subsequent use.

Preparation of DiSe@AuRod@GOD NPs (DSAG NPs): Typically, 1 mL of DSA NPs solution was centrifuged, and the resulting residue was re-dispersed in ultrapure water, to which an appropriate amount of GOD solution was added and stirred at room temperature for 30 min. 2 mg of Compound 3 was added to this solution. 0.81 mg of zinc nitrate hexahydrate dissolved

in 50 μL of ultrapure water was added dropwise to the above-mixed solution. After the dropwise addition, the solution was continued to be stirred at room temperature for 24 hours. Subsequently, the reacted solution was fully centrifuged (14 000 g, 10 min), and the collected precipitate was washed three times with ultrapure water. Finally, the precipitate obtained was dispersed in PBS solution for subsequent use.

Preparation of DiSe@AuRod@MnCO@GOD NPs (DSACG NPs): Typically, 1 mL of DSAC NPs solution was centrifuged, and the resulting residue was re-dispersed in ultrapure water, to which an appropriate amount of GOD solution was added and stirred at room temperature for 30 min. 2 mg of Compound 3 was added to this solution. 0.81 mg of zinc nitrate hexahydrate dissolved in 50 μL of ultrapure water was added dropwise to the above-mixed solution. After the dropwise addition, the solution was continued to be stirred at room temperature for 24 hours. Subsequently, the reacted solution was fully centrifuged (14 000 g, 10 min), and the collected precipitate was washed three times with ultrapure water. Finally, the precipitate obtained was dispersed in PBS solution for subsequent use.

Preparation of Cell Membrane Fragments: The preparation of cell membrane fragments is based on published articles[64]. The mouse mammary adenocarcinoma (4T1) cell membranes were obtained by a membrane protein extraction kit. Briefly, the collected cells were dispersed in membrane protein extraction buffer supplemented with PMSF and subsequently placed in an ice bath for 10-15 minutes. The cells were fragmented using a cell sonicator, so the degree of cell fragmentation was greater than 70%. The above solution was then centrifuged (700 g, 10 min) at 4°C. The supernatant was carefully taken for further centrifugation (14 000 g, 30 min), and the resulting residue was washed three times with ultrapure water. Finally, the collected precipitate was lyophilized as a 4T1 cell membrane.

Preparation of DiSe@AuRod@MnCO@GOD@Mem NPs (DSACGM NPs): The method of loading cell membranes was based on published articles[58]. 1 mL of DSACG NPs solution was centrifuged, and the obtained precipitate was redispersed in ultrapure water, mixed with the prepared cell membrane, and sonicated in an ice water bath for 20 min. Subsequently, the mixture was centrifuged (14 000 g, 10 min) to remove free cellular debris. The resulting precipitate was finally dispersed in PBS solution also for subsequent use.

Electron paramagnetic resonance (EPR) tests: The generation of ·OH was assayed using EPR. Briefly, PBS (pH 6.5) containing $NaHCO_3$ (25 mM), H_2O_2 (10 mM), glucose (4.5 g/mL), and nanoparticles (50 μg/mL) was stirred at room temperature for 30 min. Subsequently, DMPO (10 mg/mL) was added to the mixed solution and assayed by EPR spectroscopy.

Calculation of Photothermal Conversion Efficiency of the DSACGM NPs: The photothermal

conversion efficiency (η) of DSACGM NPs was calculated based on the temperature of DSACGM NPs solution (400 μg/mL) over time, which was continuously irradiated by a 1064 nm laser (1.0 W/cm^2) for 720 s until the solution reached the steady-state temperature. The temperature was detected by using an IR thermal imager. According to the method already reported[9], the η can be calculated by Eq. (1).

$$\eta = \frac{\mathrm{hS(Tmax-Tsurr)-Qdis}}{\mathrm{I(1-10^{-A1064})}} \quad (1)$$

Tmax (°C) is the equilibrium temperature, and Tsurr (°C) is the ambient temperature. Qdis the heat dissipated from the light absorbed by the solvent and the quartz cuvette. I (W/cm^2) denotes the incident laser power density. A1064 is the absorbance of the sample at 1064 nm. h (W/cm^2/K) represents the heat transfer coefficient. S (cm^2) denotes the vessel's surface area. hS the value is derived from Eq. (2-4):

$$\tau_s = \frac{m_D c_D}{\mathrm{h}S} \quad (2)$$

$$\theta = \frac{\mathrm{T-Tsurr}}{\mathrm{Tmax-Tsurr}} \quad (3)$$

$$t = -\tau_s ln\theta \quad (4)$$

Where τ_s is the time constant of heat transfer from the DSACGM NPs solution to the system, mD and cD denote the mass (1.0 g) and heat capacity (4.2 J/g/°C) of the ultrapure aqueous water used to disperse the DSACGM NPs, respectively. θ is the temperature of the introduced acausal driving force. In addition, T denotes the real-time temperature during the cooling period. Qdis calculated according to Eq. 5.

$$Q_{dis} = \frac{m_D c_D(\mathrm{Tmax}(water)-\mathrm{Tsurr})}{\tau_{water}} \quad (5)$$

Detect CO release in vitro by Hemoglobin: The concentration of CO in PBS was determined using the hemoglobin (Hb) method according to the Beer-Lambert law. Haemoglobin (Hb) has a very high affinity for carbon monoxide (CO) and can be detected spectrophotometrically as carbon oxyhemoglobin (HbCO) conjugate. Bovine hemoglobin (5 ml, 1.47 μM) was first dissolved in PBS (pH 6.5) in an N_2 atmosphere and subsequently reduced by the addition of sodium dithionite (0.4 mg/mL). Different concentrations of DSAC NP solutions were taken and added to Hb solution containing H_2O_2 (1 mM) and immediately sealed in a quartz vial. After sufficient reaction, the UV absorption values of the reaction solutions were tested.

In order to quantify the concentration of CO, we performed the following calculations:

$$\begin{cases} A_{420} = \varepsilon_{420}^{HbCO} bc_{HbCO} + \varepsilon_{420}^{Hb} bc_{Hb} \\ A_{430} = \varepsilon_{430}^{Hb} bc_{Hb} + \varepsilon_{430}^{HbCO} bc_{HbCO} \end{cases}$$

Firstly, based on the above system of equations, we can get Eq. 6:

$$c_{CO} = c_{HbCO} = c_0 \frac{\varepsilon_{430}^{Hb} A_{420} - \varepsilon_{420}^{Hb} A_{430}}{\left(\varepsilon_{430}^{Hb} - \varepsilon_{430}^{HbCO}\right) A_{420} + \left(\varepsilon_{420}^{HbCO} - \varepsilon_{420}^{Hb}\right) A_{430}} \quad (6)$$

By measuring the UV absorption of different concentrations of Hb and HbCO, the corresponding molar extinction coefficients can be calculated:

ε_{430}^{Hb}= 0.3653±0.013 cm^{-1} μM^{-1}

ε_{430}^{HbCO}= 0.2687±0.059 cm^{-1} μM^{-1}

ε_{420}^{Hb}= 0.2967±0.010 cm^{-1} μM^{-1}

ε_{420}^{HbCO}= 0.65±0.047 cm^{-1} μM^{-1}

Based on the above results, the formula for the concentration of CO can be simplified as:

$$c_{CO} = c_0 \frac{365.3A_{420} - 296.7A_{430}}{96.7A_{420} + 353.4A_{430}}$$

where c_0= 1.47 μM, and A 420 nm and A430 nm represent the absorption intensity of the reaction mixture at 410 nm and 430 nm, respectively.

Characterization of motion behavior of nanomotors: The nanomotor was loaded with RhB to facilitate the observation of the motion behavior of the nanomotor under a confocal microscope (Axio Observer.Z1/7, Plan-Apochromat 63×/1.40 Oil DIC M27), and the duration of the recording was 23.95s (150 frames). The aqueous solution containing the nanomotor was placed on a slide, and then the sample was covered with a coverslip to avoid artifacts caused by drift. Then, the CUDA Spot Tracker analysis software was used to study the particle trajectory. These tracking data were utilized in conducting mathematical statistics and motion analysis, the mean-square-displacement (MSD) of nanomotors was calculated using the formula: MSD (Δt) = $[(x_i (t + \Delta t) - x_i(t))^2$ (i =2, for two-dimensional analysis)[65,66], i is an index to show x and y, and Δt represents the time interval. Deff (the diffusion coefficient)[67] = MSD/4Δt.

Glucose oxidase activity test: Glucose oxidase catalyzes the reaction of glucose to produce gluconic acid and hydrogen peroxide while consuming oxygen in solution, so we used a dissolved oxygen meter (JBSJ-605F) to monitor the change of oxygen content in solution to determine the activity of glucose oxidase. GOD and DSACG were mixed in different glucose concentrations (0, 0.4,0.8, 2,4,6, and 8 mg/mL) in NaAc-HAc buffer solution (5 mL, 0.01 M,

pH = 6.5). Changes in oxygen concentration were recorded in real-time for 3 min. The maximum reaction rate (Vmax) and the Michaelis-Menten constant (Km) of GOD could be calculated according to the Michaelis-Menten equations (7, 8). [S] is the substrate content.

$$\frac{1}{v} = \frac{K_m}{V_{max}} \cdot \frac{1}{[S]} + \frac{1}{V_{max}} \quad (7)$$

$$V_{max} = k_{cat} \cdot [E_0] \quad (8)$$

Confocal fluorescence analysis of CO release in cells: 4T1 cells were cultured in 8-well plates (12,000 cells per well, 200 μL DMEM medium). 4T1 cells were incubated with MnCO, DSACM, and DSACGM NPs for two hours. Then, FL-CO-1 (1μM) and $PdCl_2$ (1μM) was added and incubated at 37°C for 30 min. The cells were washed three times with PBS, and the fluorescent signals were collected under a confocal microscope.

Intracellular determination of ROS: The production of reactive oxygen species is monitored using 2',7'-dichlorofluorescein diacetate (DCFH-DA), which reacts with intracellular free radicals and produces a fluorescent product, dichlorofluorescein (DCF). The intensity of the DCF fluorescence is related to the amount of reactive oxygen species in the cell. To perform the experiment, the 4T1 cells were seeded in a 6 well plate and cultured for 24 h. The cell medium was removed, and then adherent cells were incubated with DSACGM NPs (2.0, 4.0, 6.0 μg·mL^{-1}) for 8 h at 37 ℃. Before use, the adherent cells were washed three times with PBS (pH 7.4) to remove the excess NPs. DCFH-DA solution was added to the 4T1 cells, and the mixture was incubated at 37 ℃ for 0.5 h. The cells were washed three times with PBS, and the fluorescent signals were collected under a confocal microscope.

Detection of intracellular H2O2 levels: 4T1 cells were seeded in 6 well plates at a density of 1×10^5 cells/well and adhered for 24 hours. 4T1 cells were incubated under different conditions (1. UT (untreated), 2. DSACM NPs (2 μg/mL), 3. DSACM NPs (4 μg/mL), 4. DSACM NPs (6 μg/mL)) for 8h. DCFH-DA solution was added to the 4T1 cells, and the mixture was incubated at 37 ℃ for another 1 h. Finally, the cells were imaged by confocal microscopy.

To quantify the amount of H_2O_2 in the cells, we used a hydrogen peroxide detection kit (S0038, Beyotime Biotechnology) to determine the level of hydrogen peroxide in the cells. According to the kit's operating manual, the standard curve of hydrogen peroxide was first determined (Figure S22), and then the H_2O_2 levels in different groups of cells were measured.

Determination of intracellular GSH levels: 4T1 cells were seeded in 6 well plates at a density of 1×10^5 cells/well and adhered for 24 hours. 4T1 cells were incubated under different conditions (1. UT (untreated), 2. Hes NPs (60 μg/mL), 3. Cys NPs (60 μg/mL), 4. DSe NPs (60

μg/mL), 5 DSe NPs (25 μg/mL), DSe NPs (50 μg/mL), DSe NPs (100 μg/mL)) for 8h. The 4T1 cells were digested with trypsin and washed three times with PBS. 4T1 cells were tested for intracellular GSH content according to the operating method of the Reduced GSH Content Assay Kit (BL874B, Biosharp).

Determination of intracellular Glu levels: 4T1 cells were seeded in 6 well plates at a density of 1×10^5 cells/well and adhered for 24 hours. 4T1 cells were incubated under different conditions (1. UT (untreated), 2. DSACGM NPs (2 μg/mL), 3. DSACGM NPs (4 μg/mL), 4. DSACGM NPs (8 μg/mL) for 8h. The 4T1 cells were digested with trypsin and washed three times with PBS. 4T1 cells were tested for intracellular Glu content according to the operating method of the Glucose Assay Kit with O-toluidine (S0201M, Beyotime).

Detection of HSP-70 by ELISA Kit: To measure the expression level of HSP70. 4T1 cells were seeded in 6 well plates at a density of 1×10^5 cells/well and adhered for 24 hours. 4T1 cells were incubated under different conditions (1. UT (untreated), 2. NIR II, 3. 43℃, 4. DSAM NPs (2 μg/mL) + 43℃, 5. DSACM NPs (2 μg/mL) + 43℃, 6. DSACGM NPs (2 μg/mL) + 43℃, 7. DSAM NPs (2 μg/mL) + NIR II, 8. DSACM NPs (2 μg/mL) + NIR II, 9. DSACGM NPs (2 μg/mL) + NIR II). The laser's optical power density was 1.0 w/cm^2, and the illumination time was 3 min. The temperature was detected by IR thermography, and the temperature of the experimental group was controlled to be around 43℃. Cells were collected and washed three times with PBS. The HSP70 content of the cells was tested according to the instructions of the Mouse HSP70 ELISA Kit (ED-20578, LunChangShuoBiotech).

Dead/Live Staining and cell apoptosis analysis: 4T1 cells were cultured in 8-well plates (12,000 cells per well, 200 μL DMEM medium). 4T1 cells were incubated under different conditions (UT (untreated), NIR II, DSeM NPs (2 μg/mL), DSAM NPs (2 μg/mL), DSACM NPs (2 μg/mL), DSACGM NPs (2 μg/mL), DSACGM NPs (2 μg/mL) + NIR II) for 24 hours. The laser's optical power density was 1.0 w/cm^2, and the illumination time was 3 min. The temperature was detected by IR thermography, and the temperature of the experimental group was controlled to be around 43℃. Then, the cells were washed three times with PBS and co-staining with calcein-AM and PI. Finally, the cells were imaged by confocal microscopy. Flow cytometry was conducted for cell apoptosis analysis. The treated cells were collected by centrifugation. Then, the Annexin V-FITC/PI Apoptosis Detection Kit was used to stain the cells for 20 min before the flow cytometry analysis.

JC-1 Mitochondrial Membrane Potential: The mitochondrial membrane potential (MMP, ΔΨm) was measured with a MMP assay kit using JC-1 as a fluorescent probe. 4T1 cells were cultured in 8-well plates (12,000 cells per well, 200 μL DMEM medium). 4T1 cells were

incubated under different conditions (UT (untreated), NIR II, DSeM NPs (2 μg/mL), DSAM NPs (2 μg/mL), DSACM NPs (2 μg/mL), DSACGM NPs (2 μg/mL), DSACGM NPs (2 μg/mL) + NIR II) for 24 hours. The laser's optical power density was 1.0 w/cm^2, and the illumination time was 3 min. The temperature was detected by IR thermography, and the temperature of the experimental group was controlled to be around 43℃. Then, the cells were washed three times with PBS and 0.5 ml of JC-1 working solution was added and incubated for 20 minutes at 37°C in the dark. Cells were washed and resuspended with JC-1 buffer. Finally, the cells were imaged by confocal microscopy. The MMP of cells were identified by a flow cytometer.

In vivo anti-tumor effect: 4T1 tumor-bearing BALB/c mice were assigned into 7 groups (five mice each group): (1) PBS; (2) PBS + NIR II 1.0 W/cm^2 for 3 min; (3) DSAM NPs; (4) DSACM NPs; (5) DSAGM NPs; (6) DSACGM NPs; (7) DSACGM NPs + NIR II 1.0 W/cm^2 for 3 min. These mice were injected through a tail vein. After 10 h, the tumor region was irradiated by 1064 nm NIR II. The temperature was detected by IR thermography, and the temperature of the experimental group was controlled to be around 43℃. The tumor volumes and weight of mice were recorded every 2 days.

Detection of intratumoral GSH levels: Each tumor sample, weighing 0.1g, was homogenized in 1mL extraction buffer using a glass homogenizer on an ice bath. After centrifugation (12000 rpm, 4℃, 15 min), the supernatant was collected and kept on ice until analysis. After extracting all samples, GSH content was measured according to the instructions in the Reduced GSH Content Assay Kit (BL874B, Biosharp).

Detection of intratumoral glu levels: Each tumor sample, weighing 0.1g, was homogenized in 1mL lysis buffer using a glass homogenizer on an ice bath. After centrifugation (12000 rpm, 4℃, 15 min), the supernatant was collected and kept on ice until analysis. After extracting all samples, Glu content was measured according to the instructions in the Glucose Assay Kit with O-toluidine (S0201M, Beyotime).

H&E and TUNEL staining: Major organs and tumors were excised from mice 14 days after injection. Collected tumors and organs were fixed with 4% paraformaldehyde, paraffin-embedded, sectioned at ~ 4.0 μm, and stained with H&E. In addition, tumor sections were stained with TUNEL to determine the apoptosis of tumor cells according to the one-step TUNEL Apoptosis Detection Kit. Samples were examined with an Olympus IX73 microscope and CLSM.

Supporting Information

Supporting Information is available from the Wiley Online Library or from the author.

Acknowledgements

This work was supported by the National Key R&D Program of China (2020YFA0908500), the National Natural Science Foundation of China (22161142015, 22201058, and 22275046), the Inter- disciplinary Research Project of Hangzhou Normal University (2024JCXK01), and the Hangzhou Leading Innovation and Entrepreneurship Team Project of Hangzhou Science and Technology Bureau (TD2022001).

Conflict of Interest

The authors declare no conflict of interest.

Data Availability Statement

The data that support the findings of this study are available from the corresponding author upon reasonable request.

Received: ((will be filled in by the editorial staff))
Revised: ((will be filled in by the editorial staff))
Published online: ((will be filled in by the editorial staff))

References

[1] J. Ferlay, M. Colombet, I. Soerjomataram, D. M. Parkin, M. Piñeros, A. Znaor, F. Bray, *Int. J. Cancer* **2021**, *149*, 778.

[2] H. Sung, J. Ferlay, R. L. Siegel, M. Laversanne, I. Soerjomataram, A. Jemal, F. Bray, *CA Cancer J. Clin.* **2021**, *71*, 209.

[3] R. L. Siegel, K. D. Miller, N. S. Wagle, A. Jemal, *CA Cancer J. Clin.* **2023**, *73*, 17.

[4] Y. Sun, *Med. Res. Rev.* **2015**, *35*, DOI 10.1002/med.21338.

[5] J. Cao, D. Huang, N. A. Peppas, *Adv. Drug Deliver. Rev.* **2020**, *167*, 170.

[6] P. Gotwals, S. Cameron, D. Cipolletta, V. Cremasco, A. Crystal, B. Hewes, B. Mueller, S. Quaratino, C. Sabatos-Peyton, L. Petruzzelli, J. A. Engelman, G. Dranoff, *Nat. Rev. Cancer* **2017**, *17*, 286.

[7] W. Fan, B. Yung, P. Huang, X. Chen, *Chem. Rev.* **2017**, *117*, 13566.

[8] Z. Xie, T. Fan, J. An, W. Choi, Y. Duo, Y. Ge, B. Zhang, G. Nie, N. Xie, T. Zheng, Y. Chen, H. Zhang, J. S. Kim, *Chem. Soc. Rev.* **2020**, *49*, 8065.

[9] H. Lin, S. Gao, C. Dai, Y. Chen, J. Shi, *J. Am. Chem. Soc.* **2017**, *139*, 16235.

[10] K. Yang, S. Zhao, B. Li, B. Wang, M. Lan, X. Song, *Coordin. Chem. Rev.* **2022**, *454*, 214330.

[11] K. F. Chu, D. E. Dupuy, *Nat. Rev. Cancer* **2014**, *14*, 199.

[12] Y. Duan, H. Yang, J. Gao, D. Wei, Y. Zhang, J. Wang, X. Zhang, J. Zhang, K. Ge, X. Wu, J. Chang, *ACS Appl. Bio Mater.* **2021**, *4*, 1524.

[13] G. Gao, X. Sun, G. Liang, *Adv. Funct. Mater.* **2021**, *31*, 2100738.

[14] X. Tang, L. Tan, K. Shi, J. Peng, Y. Xiao, W. Li, L. Chen, Q. Yang, Z. Qian, *Acta Pharm. Sin. B* **2018**, *8*, 587.

[15] X. He, Y. Hao, B. Chu, Y. Yang, A. Sun, K. Shi, C. Yang, K. Zhou, Y. Qu, H. Li, Z. Qian, *Nano Today* **2021**, *39*, 101174.

[16] X. Wang, X. Zhong, Z. Liu, L. Cheng, *Nano Today* **2020**, *35*, 100946.

[17] Z. Tang, Y. Liu, M. He, W. Bu, *Angew. Chem. Int. Edit.* **2019**, *131*, 958.

[18] M. Huo, L. Wang, Y. Wang, Y. Chen, J. Shi, *ACS Nano* **2019**, *13*, 2643.

[19] Y. Cheng, Y.-D. Xia, Y.-Q. Sun, Y. Wang, X.-B. Yin, *Adv. Mater.* **2024**, *36*, 2308033.

[20] L.-S. Lin, J. Song, L. Song, K. Ke, Y. Liu, Z. Zhou, Z. Shen, J. Li, Z. Yang, W. Tang, G. Niu, H.-H. Yang, X. Chen, *Angew. Chem. Int. Edit.* **2018**, *130*, 4996.

[21] Y. S. Choi, K. M. Huh, M. S. Shim, I. S. Park, Y.-Y. Cho, J. Y. Lee, H. S. Lee, H. C. Kang, *Adv. Funct.Mater.* **2021**, *31*, 2007275.

[22] D. Kim, K. Shin, S. G. Kwon, T. Hyeon, *Adv. Mater.* **2018**, *30*, 1802309.

[23] D. Peer, J. M. Karp, S. Hong, O. C. Farokhzad, R. Margalit, R. Langer, *Nat. Nanotech.* **2007**, *2*, 751.

[24] Y. Wu, Y. Qin, M. Muppidathi, R. Carmieli, M. Fadeev, W. Lei, M. Xia, I. Willner, *Adv. Funct. Mater.* **2024**, *34*, 2306929.

[25] G. Zhou, M. Li, *Adv. Materi.* **2022**, *34*, 2200871.

[26] Q. Zhang, G. Kuang, H. Wang, Y. Zhao, J. Wei, L. Shang, *Adv. Sci.* **2023**, *10*, 2303818.

[27] H. Zhu, F. Gao, Y. Li, M. Jiang, Y. Zhang, C. Kan, L. Han, S. Xue, K. Wang, Q. Fan, H. Hu, F. Sun, Z. Ming, *Nano Today* **2024**, *56*, 102308.

[28] J. Liu, T. Liu, P. Du, L. Zhang, J. Lei, *Angew. Chem. Int. Edit.* **2019**, *58*, 7808.

[29] C. Fang, Z. Deng, G. Cao, Q. Chu, Y. Wu, X. Li, X. Peng, G. Han, *Adv. Funct. Mater.* **2020**, *30*, 1910085.

[30] Y. Liu, H. Wu, S. Wang, X. Zhang, L. Gong, C. Xiao, C. Liu, L. Chen, H. Zhao, C. Liu, M. Jin, Z. Gao, W. Huang, *Mater. Today* **2023**, *68*, 125.

[31] Y. Boucher, L. T. Baxter, R. K. Jain, *Cancer Res.* **1990**, *50*, 4478.

[32] Q. Dai, S. Wilhelm, D. Ding, A. M. Syed, S. Sindhwani, Y. Zhang, Y. Y. Chen, P. MacMillan, W. C. W. Chan, *ACS Nano* **2018**, *12*, 8423.

[33] E. Blanco, H. Shen, M. Ferrari, *Nat. Biotechnol.* **2015**, *33*, 941.

[34] M. Pacheco, B. Jurado-Sánchez, A. Escarpa, *Angew. Chem. Int. Edit.* **2019**, *131*, 18185.

[35] A. C. Hortelão, T. Patiño, A. Perez-Jiménez, À. Blanco, S. Sánchez, *Adv. Funct. Mater.* **2018**, *28*, 1705086.

[36] M. Pal, N. Somalwar, A. Singh, R. Bhat, S. M. Eswarappa, D. K. Saini, A. Ghosh, *Adv. Mater.* **2018**, *30*, 1800429.

[37] X. Lin, Z. Wu, Y. Wu, M. Xuan, Q. He, *Adv. Mater.* **2016**, *28*, 1060.

[38] J. Shao, S. Cao, D. S. Williams, L. K. E. A. Abdelmohsen, J. C. M. van Hest, *Angew. Chem. Int. Edit.* **2020**, *59*, 16918.

[39] C. Gao, Y. Wang, Z. Ye, Z. Lin, X. Ma, Q. He, *Adv. Mater.* **2021**, *33*, 2000512.

[40] M. Xuan, J. Shao, C. Gao, W. Wang, L. Dai, Q. He, *Angew. Chem. Int. Edit.* **2018**, *57*, 12463.

[41] L. Ren, W. Wang, T. E. Mallouk, *Acc. Chem. Res.* **2018**, *51*, 1948.

[42] J. Guo, J. J. Gallegos, A. R. Tom, D. Fan, *ACS Nano* **2018**, *12*, 1179.

[43] M. Pal, N. Somalwar, A. Singh, R. Bhat, S. M. Eswarappa, D. K. Saini, A. Ghosh, *Adv. Mater.* **2018**, *30*, 1800429.

[44] L. K. E. A. Abdelmohsen, M. Nijemeisland, G. M. Pawar, G.-J. A. Janssen, R. J. M. Nolte, J. C. M. van Hest, D. A. Wilson, *ACS Nano* **2016**, *10*, 2652.

[45] A. C. Hortelão, S. García-Jimeno, M. Cano-Sarabia, T. Patiño, D. Maspoch, S. Sanchez, *Adv. Funct. Mater.* **2020**, *30*, 2002767.

[46] Y. Yang, X. Arqué, T. Patiño, V. Guillerm, P.-R. Blersch, J. Pérez-Carvajal, I. Imaz, D. Maspoch, S. Sánchez, *J. Am. Chem. Soc.* **2020**, *142*, 20962.

[47] L. Liu, S. Li, K. Yang, Z. Chen, Q. Li, L. Zheng, Z. Wu, X. Zhang, L. Su, Y. Wu, J. Song, *Nano Lett.* **2023**, *23*, 3929.

[48] Y. Lu, S. Liu, J. Liang, Z. Wang, Y. Hou, *Adv. Healthcare Mater.* **2024.**, *13*, 2304212.

[49] H. Chen, T. Li, Z. Liu, S. Tang, J. Tong, Y. Tao, Z. Zhao, N. Li, C. Mao, J. Shen, M. Wan, *Nat. Commun.* **2023**, *14*, 941.

[50] S. Zheng, Y. Wang, S. Pan, E. Ma, S. Jin, M. Jiao, W. Wang, J. Li, K. Xu, H. Wang, *Adv. Funct. Mater.* **2021**, *31*, 2100936.

[51] M. Zhu, L. Zhu, Y. You, M. Sun, F. Jin, Y. Song, J. Zhang, X. Xu, J. Ji, Y. Du, *ACS Nano* **2023**, *17*, 17285.

[52] Y. Xing, J. Xiu, M. Zhou, T. Xu, M. Zhang, H. Li, X. Li, X. Du, T. Ma, X. Zhang, *ACS Nano* **2023**, *17*, 6789.

[53] J. Yu, Y. Li, A. Yan, Y. Gao, F. Xiao, Z. Xu, J. Xu, S. Yu, J. Liu, H. Sun, *Adv. Sci.* **2023**, *10*, 2301919.

[54] M. Wan, Q. Wang, X. Li, B. Xu, D. Fang, T. Li, Y. Yu, L. Fang, Y. Wang, M. Wang, F. Wang, C. Mao, J. Shen, J. Wei, *Angew. Chem. Int. Edit.* **2020**, *59*, 14458.

[55] G. Ma, Z. Liu, C. Zhu, H. Chen, R. T. K. Kwok, P. Zhang, B. Z. Tang, L. Cai, P. Gong, *Angew. Chem. Int. Edit.* **2022**, *61*, e202207213.

[56] Y. Pan, K. Sun, S. Liu, X. Cao, K. Wu, W.-C. Cheong, Z. Chen, Y. Wang, Y. Li, Y. Liu, D. Wang, Q. Peng, C. Chen, Y. Li, *J. Am. Chem. Soc.* **2018**, *140*, 2610.

[57] J. Yang, F. Zhang, H. Lu, X. Hong, H. Jiang, Y. Wu, Y. Li, *Angew. Chem. Int. Edit.* **2015**, *54*, 10889.

[58] Y. Gan, W. Xie, M. Wang, P. Wang, Q. Li, J. Cheng, M. Yan, J. Xia, Z. Wu, G. Zhang, *Mater. Today Bio.* **2024**, *24*, 100941.

[59] Y. Li, J., D. Wang, J. Lv, K. Hou, Y. Liu, C. Chen, Z. Tang, *Nano Res.* **2018**, *11*, 3294.

[60] G. Zhou, M. Li, *Adv. Mater.* **2022**, *34*, 2200871.

[61] W. Liang, H. Xu, F. Carraro, N. K. Maddigan, Q. Li, S. G. Bell, D. M. Huang, A. Tarzia, M. B. Solomon, H. Amenitsch, L. Vaccari, C. J. Sumby, P. Falcaro, C. J. Doonan, *J. Am. Chem. Soc.* **2019**, *141*, 2348.

[62] J. Wu, Z. Meng, A. A. Exner, X. Cai, X. Xie, B. Hu, Y. Chen, Y. Zheng, *Biomaterials* **2021**, *276*, 121001.

[63] L.-S. Lin, J. Song, L. Song, K. Ke, Y. Liu, Z. Zhou, Z. Shen, J. Li, Z. Yang, W. Tang, G. Niu, H.-H. Yang, X. Chen, *Angew. Chem. Int. Edit.* **2018**, *57*, 4902.

[64] S.-Y. Li, H. Cheng, B.-R. Xie, W.-X. Qiu, J.-Y. Zeng, C.-X. Li, S.-S. Wan, L. Zhang, W.-L. Liu, X.-Z. Zhang, *ACS Nano* **2017**, *11*, 7006.

[65] G. Dunderdale, S. Ebbens, P. Fairclough, J. Howse, *Langmuir* **2012**, *28*, 10997.

[66] M. Luo, S. Li, J. Wan, C. Yang, B. Chen, J. Guan, *Langmuir* **2020**, *36*, DOI 10.1021/acs.langmuir.9b03315.

[67] Y. Xing, M. Zhou, T. Xu, S. Tang, Y. Fu, X. Du, L. Su, Y. Wen, X. Zhang, T. Ma, *Angew. Chem. Int. Edit.* **2020**, *59*, 14368.